Phase formation and thermal analysis in the LaPO$_4$–GdPO$_4$–H$_2$O system

Maria O. Enikeeva[1,2,a], Kseniya A. Zhidomorova[2,3,b], Dmitriy P. Danilovich[3,c],
Vladimir N. Nevedomskiy [1,d], Olga V. Proskurina[1,3,e], Victor V. Gusarov[1,f]

[1]Ioffe Institute, St. Petersburg, Russia

[2]Branch of Petersburg Nuclear Physics Institute named after B.Ṗ. Konstantinov of National Research Centre
"Kurchatov Institute" – Institute of Silicate Chemistry, St. Petersburg, Russia

[3]St. Petersburg State Institute of Technology, St. Petersburg, Russia

[a]i@odin2tri.ru, [b]zhidomorovak@gmail.com, [c]dmitrydanilovich@gmail.com,
[d] nevedom@mail.ioffe.ru, [e]proskurinaov@mail.ioffe.ru, [f]gusarov@mail.ioffe.ru

Corresponding author: M. O. Enikeeva, i@odin2tri.ru

ABSTRACT Structural transformations of nanocrystals in the LaPO$_4$–GdPO$_4$–(H$_2$O) system under hydrothermal conditions at 230 °C were studied depending on the duration of isothermal holding (2 hours, 3 days, and 5 days). It has been shown that a phase with the rhabdophane-like structure, La$_{1-x}$Gd$_x$PO$_4 \cdot n$H$_2$O (0.00$\leq x \leq$1.00), exhibits a weighted average crystallite size of 4–7 nm and crystallizes in the system prior to hydrothermal treatment. As a result of hydrothermal treatment, samples in the LaPO$_4$–GdPO$_4$–(H$_2$O) system are completely transformed into a phase with a monazite structure within five days, with the slowest transformation observed for gadolinium orthophosphate. It was found that nanoparticles with a rhabdophane structure, GdPO$_4 \cdot n$H$_2$O, possess a single-crystal structure. The thermal analysis data indicated that the samples obtained via the precipitation method contain an X-ray amorphous phase and impurity compounds. The onset temperature of the structural transformation from rhabdophane to monazite, as well as the number of water molecules in the rhabdophane-like structure, depends on the chemical composition of the compound, particularly with regard to the isomorphic substitution of lanthanum cations with gadolinium cations.

KEYWORDS solid solution, rhabdophane structure, thermal analysis, structural transformations.

1. Introduction

Orthophosphates of rare earth elements (REE), represented as REEPO$_4$, include elements ranging from lanthanum to lutetium, as well as yttrium and scandium. These materials are of significant interest in modern materials science due to their potential applications in non-carbon energy fields such as catalysis [1–4], immobilization of radioactive waste [5–8], various types of luminescence [9–13], and thermal barrier coatings [14–17]. Compounds with monazite and xenotime structures exhibit high chemical and radiation resistance [18–23], a high melting point [24–26], and a diverse chemical composition [27–31]. In addition to the anhydrous phases with monazite and xenotime structures, REE orthophosphates can form hydrated structures – rhabdophane and churchite, which are often considered precursor phases to the anhydrous compounds [32–35]. Compounds with the churchite structure, HREEPO$_4$·2H$_2$O, are layered orthophosphates of heavy rare earth elements (HREE: elements from gadolinium to lutetium and yttrium). In the churchite structure, each layer comprises a two-dimensional framework of yttrium atoms coordinated to phosphate groups through oxygen atoms, with water molecules coordinated to the yttrium atoms and located on the outer sides of the layers. The churchite structure contains two water molecules per formula unit, as confirmed by thermal analysis studies [33,36], and serves as a structural analogue of gypsum (CaSO$_4$·2H$_2$O) [37, 38].

The structure of rhabdophane (REEPO$_4 \cdot n$H$_2$O) is known to contain quasi-one-dimensional channels that include water molecules. Compounds with the rhabdophane-like structure are typically synthesized in a single step using soft chemistry methods, such as precipitation [27, 34, 39] and hydrothermal treatment [34, 40–43]. Early X-ray structural analysis indicated that the structure of rhabdophane (REEPO$_4 \cdot n$H$_2$O) for REE = La, Ce, and Nd could be described as having hexagonal symmetry in the space group $P6_2$22 (180) [44, 45]. However, this description does not account for the

presence of water molecules within the unit cell. Subsequent analysis [41, 46] prompted a revision of the space group for rhabdophane, changing it from hexagonal $P6_222$ to monoclinic $C2$ (5) for the hydrated compound, and to trigonal $P3_121$ (152) for the anhydrous form [41]. The monoclinic model describing rhabdophane in the space group $C2$ contains channels oriented along the [101] direction, which are formed by the contact between the edges of the REE polyhedra and PO_4 tetrahedra. This structural description assumes the presence of channels within the unit cell, rather than at the boundaries, as indicated by the hexagonal model. The determined values for the number of water molecules in the rhabdophane structure (C2) are $n=2/3\approx0.67$ or $n=1/2\approx0.50$ per formula unit of the compound, and the crystal chemical structure resembles $CaSO_4 \cdot 0.5H_2O$ [47]. It should be noted separately that refining the number of water molecules in the rhabdophane structure using electron diffraction does not yield exact answers regarding their quantity, positional occupancy, or atomic coordinates.

Electron single-crystal diffraction data for a single crystal of $DyPO_4 \cdot nH_2O$ with the rhabdophane-like structure indicate that the hydrated structure can be described using a trigonal lattice of space group $P3_121$, exhibiting an effective doubling of the unit cell compared to the original Mooney description in [44, 45]. Moreover, there is a significant shift in the ion positions within the unit cell [48]. In the work [41], it is suggested that the channel size of the rhabdophane structure depends on the ionic radius of the rare earth element (REE) and affects the amount of structurally bound water: the smaller the ionic radius, the lower the unit cell volume and, consequently, the lower the water content in the structure. Additionally, the role of water in stabilizing the rhabdophane structure is discussed, with the assumption that water present in the channels helps stabilize the structure; its loss can lead to a monotropic transition to the monazite structure [42, 49]. A primary challenge in describing the structure of rhabdophane arises from the water molecules that are part of the compound; these molecules are not easily localized within the unit cell, and their locations can vary randomly among several equivalent positions in the structure [48].

One of the approaches for quantitatively describing the water content in the rhabdophane structure involves thermal analysis methods such as DTA/DSC/TG. Despite the uncertainties inherent in thermal analysis data – such as the superposition of various stages of mass loss, thermal effects associated with the removal of adsorbed water or water from structural channels, and the decomposition of reaction by-products and surfactants [50–53], these methods are widely applicable in the study of hydrated compounds [33, 42, 54, 55]. Data on the thermal behavior of the rhabdophane structure are presented in references [42, 53, 56, 57] and pertain to the determination of the thermodynamic characteristics of individual compounds, with less frequent studies on phases of variable composition [43, 46]. Furthermore, investigating the rhabdophane structure with variable composition could contribute to developing a unified concept of "the role of water in hydrated compounds with the rhabdophane-like structure", which would be valuable for the creation of new functional materials.

To obtain hydrated phases and investigate the phase formation of complex oxide systems, various soft chemistry approaches are employed [58]. This group of methods enables phase formation processes to occur at relatively low temperatures, making it particularly applicable to hydrated compounds and often utilized for the synthesis of nanomaterials [59–61].

As a result, the present work aims to study the formation process of nanocrystalline orthophosphates with variable composition in the $LaPO_4$–$GdPO_4$–H_2O system using soft chemistry methods. Additionally, it seeks to examine the thermal behavior of the resulting compounds composed of nanocrystalline particles with a rhabdophane-like structure.

2. Materials and methods

For the synthesis of $La_{1-x}Gd_xPO_4 \cdot (nH_2O)$ samples (x=0.00, 0.20, 0.50, 0.75, 0.85, 1.00), hexahydrate nitrates of rare earth elements (chemically pure) and ammonium dihydrogen phosphate (chemically pure) were used. Precipitation was carried out by adding an aqueous solution of $NH_4H_2PO_4$ to an aqueous solution of REE nitrates while continuously stirring at a temperature of 25 ± 5 °C. The resulting white suspension with a pH of 1 was stirred for 15 minutes.

For synthesis under hydrothermal conditions, the suspension obtained by precipitation was placed in a Teflon ampoule of a laboratory autoclave (fill factor 0.7) and treated hydrothermally at 230 °C and $\sim$10 MPa, with isothermal holding times of 2 hours, 3 days, and 5 days.

All samples obtained were washed with distilled water until a pH of 7 was achieved, precipitated by centrifugation (10,000 rpm), dried at 75–80 °C for 24 hours, and milled in an agate mortar.

SEM images and elemental composition of the samples were obtained using a Tescan Vega 3 SBH scanning electron microscope (Tescan, Czech Republic) equipped with an Oxford Instruments INCA x-act attachment (Oxford Instruments, UK). The images of the samples were recorded using secondary electron detectors. Composition analysis was performed on 4–5 different areas, averaging the obtained values.

The study of the crystal structure and microstructure of the samples was conducted using transmission electron microscopy (TEM) on a JEM-2100F microscope (JEOL Ltd., Akishima, Tokyo, Japan) operating at an accelerating voltage of 200 kV.

Diffraction studies were carried out using a DRON-8N X-ray powder diffractometer (Bourevestnik, JSC, Russia) under Bragg-Brentano geometry conditions and an X-ray tube with a copper anode (K_α doublet) equipped with Goebel parabolic mirrors at the primary beam output. Data collection was performed for the Bragg angle (2θ) ranging from 10 to

90° with a step of 0.01° in exposure mode with a shutter speed of 7 s. Phase analysis of the samples was conducted using PDF-2 and CCDC databases. Full-profile phase analysis was performed using SmartLab Studio II v4.4.241.0 software (Rigaku Corporation, Japan) using the Rietveld method [62]. The weighted average values of crystallite sizes were calculated in accordance with the lognormal distribution law for non-overlapping reflections of each phase: reflection 200 was used for the phase with the monazite-like structure and reflection $11\bar{1}$ for the phase with the rhabdophane-like structure.

Differential thermal analysis and thermogravimetry (DTA/TG) was performed using a Shimadzu DTG-60 (Shimadzu, Japan) with a heating rate of 10 °C/min in air. The first part of the experiment was conducted on all $La_{1-x}Gd_xPO_4 \cdot nH_2O$ samples (x=0.00, 0.20, 0.50, 0.75, 0.85, 1.00) obtained by precipitation, covering a temperature range from 25 to 1000 °C.

In the second part, the samples underwent preliminary heat treatment in a muffle furnace at the same heating rate: for 3 minutes at 300 °C for the $LaPO_4 \cdot nH_2O$ sample and for 10 minutes at 400 °C for the $GdPO_4 \cdot nH_2O$ sample. After isothermal holding, the samples were removed from the furnace, allowed to cool spontaneously to room temperature, ground again in an agate mortar, and then examined by X-ray diffraction to determine the phase composition. Following this procedure, DTA/TG of the samples was conducted at a heating rate of 10 °C/min in dynamic mode over the range from 25 to 1000 °C, as well as in quasi-static mode from 25 to 500 °C. The temperature steps for the quasi-isothermal mode were chosen to initiate the dehydration of the rhabdophane-like structure at each temperature step.

3. Results and discussion

3.1. Phase formation in LaPO₄–GdPO₄–H₂O system

Based on the results of energy dispersive X-ray, the ratio (La + Gd) : P was found to be approximately 1:1, which corresponds to the stoichiometry of REE orthophosphate. The experimentally determined molar fraction of gadolinium orthophosphate (x) in the compound $La_{1-x}Gd_xPO_4 \cdot (nH_2O)$ is used to designate the samples. The results of the elemental analysis, which reflect the content of $GdPO_4$ in the system, are presented in Table S1.

The X-ray diffraction patterns of the samples obtained via the precipitation method are shown in Fig. 1. All samples crystallize in the rhabdophane-like structure (space group $C2$). The X-ray diffraction patterns for the samples produced using hydrothermal treatment are presented in figs. S1–S3 in the Supplementary Materials. The results of quantitative phase analysis for samples synthesized under hydrothermal conditions for 2 hours and 3 days are shown in Fig. 2. After 2 hours of isothermal holding in the hydrothermal fluid, the phase with the rhabdophane-like structure was completely transformed into the monazite-like structure for the sample with x=0.00 (Fig. 2a). Samples containing 0.20 to 0.75 mol. fr. of $GdPO_4$ transformed into the monazite phase more slowly and exhibited a mixture of phases with both monazite-like and rhabdophane-like structures. In contrast, samples x=0.85 and x=1.00 retained the rhabdophane structure. As illustrated in Fig. 2b, increasing the isothermal holding time to three days results in the formation of a wide homogeneity region of the monazite-like structure based on $La_{1-x}Gd_xPO_4$, for x from 0.00 to 0.85. Only gadolinium orthophosphate (x=1.00) contains approximately 19% of the monazite phase. After five days of isothermal holding, all samples crystallized in the monazite phase.

Fig. 3 illustrates the dependencies of the unit cell volumes of the phases with monazite and rhabdophane structures, normalized to one formula unit (V/z), for samples obtained through precipitation and hydrothermal treatment. In the samples obtained via the precipitation method, a phase of variable composition with the rhabdophane-like structure forms across the entire concentration range (Fig. 3a). As shown in Fig. 3b, after hydrothermal treatment for 2 hours, two solid solutions: one with the rhabdophane-like structure and another with the monazite-like structure are observed in the system. Notably, the transformation from the rhabdophane structure to the monazite structure appears to occur without changing the cation ratio, as indicated by the linear dependence of the V/z parameter for the rhabdophane structure on composition. The absence of data for the monazite structure in the sample x=0.75 in Fig. 3b is attributed to the small amount of the monazite phase, which are less than 5% and makes it impossible to determine the precise parameters of the unit cell. After hydrothermal treatment for 3 and 5 days (Fig. 3c,d), the chemical composition of the monazite-like phase are the same, indicating complete isomorphic substitution of cations in the $LaPO_4$–$GdPO_4$–(H_2O) system.

The dependences of the weighted average value of crystallite sizes on the composition are shown in Fig. 4 for the samples obtained by precipitation and hydrothermal treatment with different durations of isothermal holding. The precipitation method was used to obtain nanocrystalline powders with an average value of crystallite sizes of 4–7 nm for $La_{1-x}Gd_xPO_4 \cdot nH_2O$ (x=0.00–1.00) with a rhabdophane-like structure (Fig. 4a). As shown in Fig.4b, during the structural transformation in a hydrothermal fluid after 2hours of isothermal holding, the weighted average values of the crystallite sizes of the monazite structure are about 15 nm and coincide with the weighted average values of the crystallite sizes of the rhabdophane structure in the two-phase region (x=0.20–0.50). In the $La_{1-x}Gd_xPO_4 \cdot nH_2O$ (x=0.20–1.00) samples, a close to exponential nature of the dependence of the weighted average value of the crystallite sizes of the rhabdophane structure on the concentration of $GdPO_4$ in the $LaPO_4$–$GdPO_4$–H_2O system is noted. A similar dependence $D(x)$ was determined in the work devoted to the $LaPO_4$–YPO_4–H_2O system [34]. Thus, the substitution of La^{3+} ((C.N.=9) 1.216 Å) in orthophosphate for REE with a smaller ionic radius Y^{3+} ((C.N.=9) 1.075 Å) or Gd^{3+} ((C.N.=9)
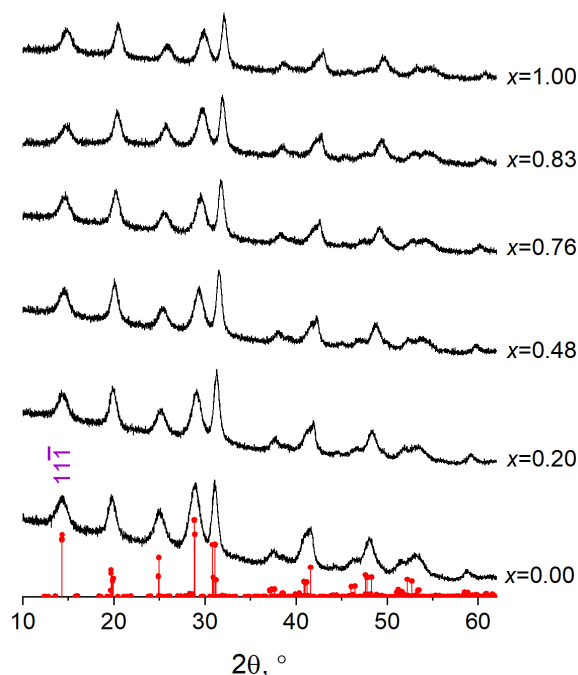
FIG. 1. Diffraction patterns of $La_{1-x}Gd_xPO_4 \cdot nH_2O$ samples obtained by precipitation. The vertical lines accompany rhabdophane-like structure (space group $C2$ [46])

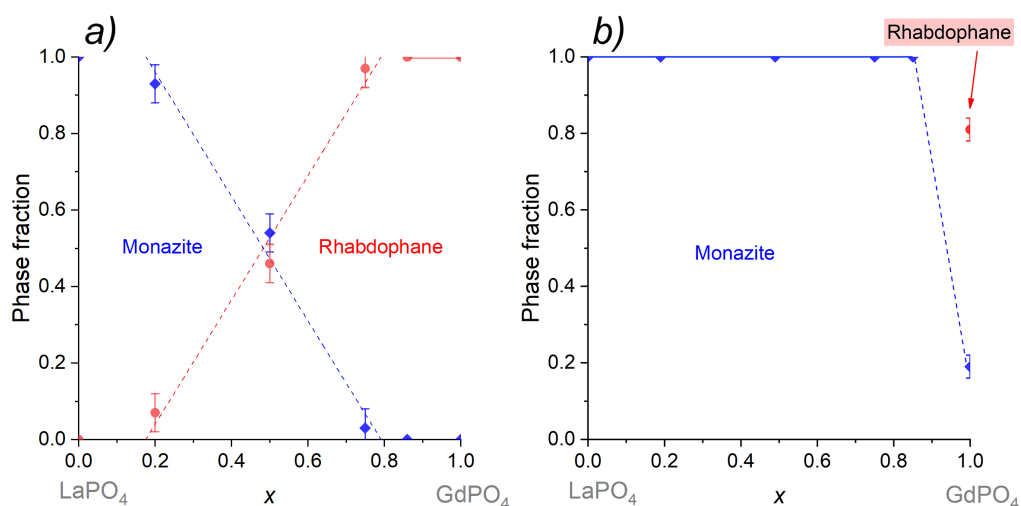FIG. 2. The phase ratio in the system for $La_{1-x}Gd_xPO_4 \cdot (nH_2O)$ samples: a) after 2 hours of isothermal holding, b) after 3 days of isothermal holding

1.107 Å), leads to a slowdown in the rhabdophane → monazite structural transformation and to an increase in the crystallite sizes of the rhabdophane structure due to recrystallization in a hydrothermal fluid. As shown in Fig. 4c, the weighted average value of the crystallite sizes of the monazite structure after 3 days of isothermal holding varies from 19 ± 10 nm for the $x=0.00$ sample to 145 ± 10 nm for the $x=1.00$ sample. The weighted average value of the crystallite sizes of the rhabdophane structure in the sample $x=1.00$ is about 100 nm, which is slightly lower than the value for the monazite structure in the same sample. This effect is probably associated with the process of transformation of the phase with the rhabdophane structure into the phase with the monazite structure, when the increase in the crystallite sizes is caused by the slow rate of structural transformation compared to the samples $0.00 \le x \le 0.85$. The data on the weighted average values of the crystallite sizes of the samples with the monazite structure obtained after 5 days of isothermal holding are shown in Fig. 4d, which, within the error, coincide with the crystallite sizes obtained after 3 days of hydrothermal treatment; the nature of the $D(x)$ dependence remains close to exponential.

Fig. 5 shows images of nanoparticles with the composition $x=1.00$ obtained by precipitation followed by heat treatment for 5 minutes at 400 °C (Fig. 5a-c) and after hydrothermal treatment for 2 hours (Fig. 5d-f). Their electron diffraction patterns are shown in Fig. 5g,h. The nanoparticles with the rhabdophane-like structure exhibit a quasi-one-dimensional
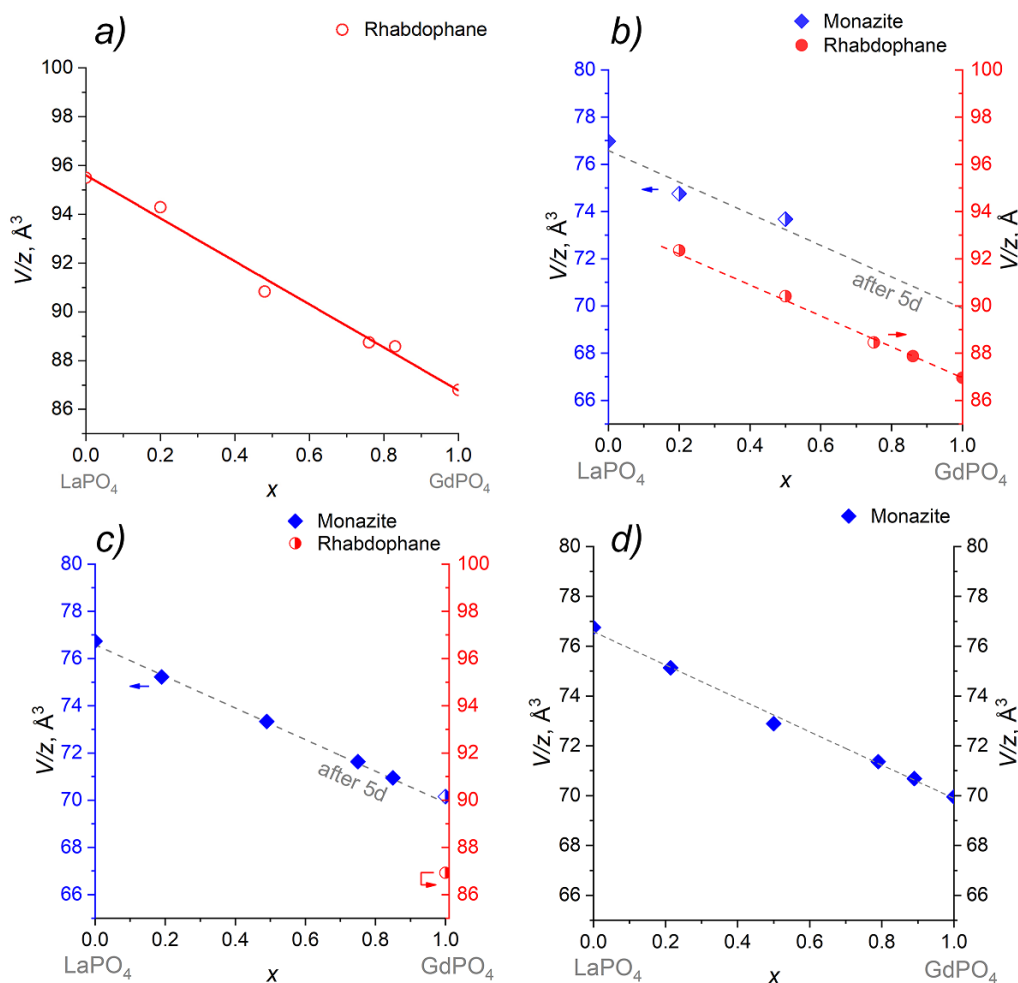
FIG. 3. Dependences of the unit cell volumes, normalized to one formula unit (V/z), on the composition of the system for phases with rhabdophane-like and monazite-like structures are presented as follows: *a*) precipitation, *b*) hydrothermal treatment for 2 hours, *c*) hydrothermal treatment for 3 days, *d*) hydrothermal treatment for 5 days

morphology. The average thickness of nanoparticles obtained by precipitation is 9±2 nm, while after hydrothermal treatment, it is 40±12 nm. The average thickness of nanoparticles in the samples correlates well with the weighted average values of crystallite sizes (Fig. 4a,b): D=6±2 nm and D=55±35 nm for the samples before and after hydrothermal treatment, respectively. The dark-field TEM images (Fig. 5b,e) indicate that the nanoparticles of the samples possess a single-crystal structure, meeting the Bragg reflection condition. Therefore, it can be concluded that the rhabdophane-like particles are single crystals. The high-resolution TEM images (Fig. 5c,f) display the average interplanar distances (d), which coincide within the margin of error with the X-ray diffraction data and are associated with the rhabdophane-like structure (space group $C2$ [41, 46]). According to the electron diffraction data, the interplanar distances for the samples with $x = 1.00$, obtained via the deposition method (Fig. 5g) and after hydrothermal treatment (Fig. 5h), differ slightly: the interplanar distances in the sample obtained by deposition followed by heat treatment for 5 minutes at 400 °C are smaller than those in the sample obtained after hydrothermal treatment. Since both samples crystallize in the same rhabdophane-like structure, the difference in d values may be attributed to the varying water content in the structure.

3.2. DTA/TG studies of samples obtained by precipitation method

Fig. 6a-f presents the DTA/TG data for the entire series of samples with x=0.00–1.00 obtained via the precipitation method. Based on changes in the slope of the tangent to the TG curve, four steps of mass loss associated with the removal of water from the samples were identified: the zero step from 25 °C to approximately 125 °C is p presumably related to the removal of water from the surface of the nanoparticles (adsorbed water), while the first, second, and third steps are associated with the removal of water from the rhabdophane-like structure. An analysis of the obtained data is presented in Table S2 and Fig. 7a,b as a function of the number of water molecules (n) in the rhabdophane structure per formula unit of the compound, as well as a dependence of the temperatures at which mass loss begins for steps 1–3 on the composition of the compound, expressed in ionic radii of the 9-coordinated REE^{3+} ion. The studied samples can be divided into two
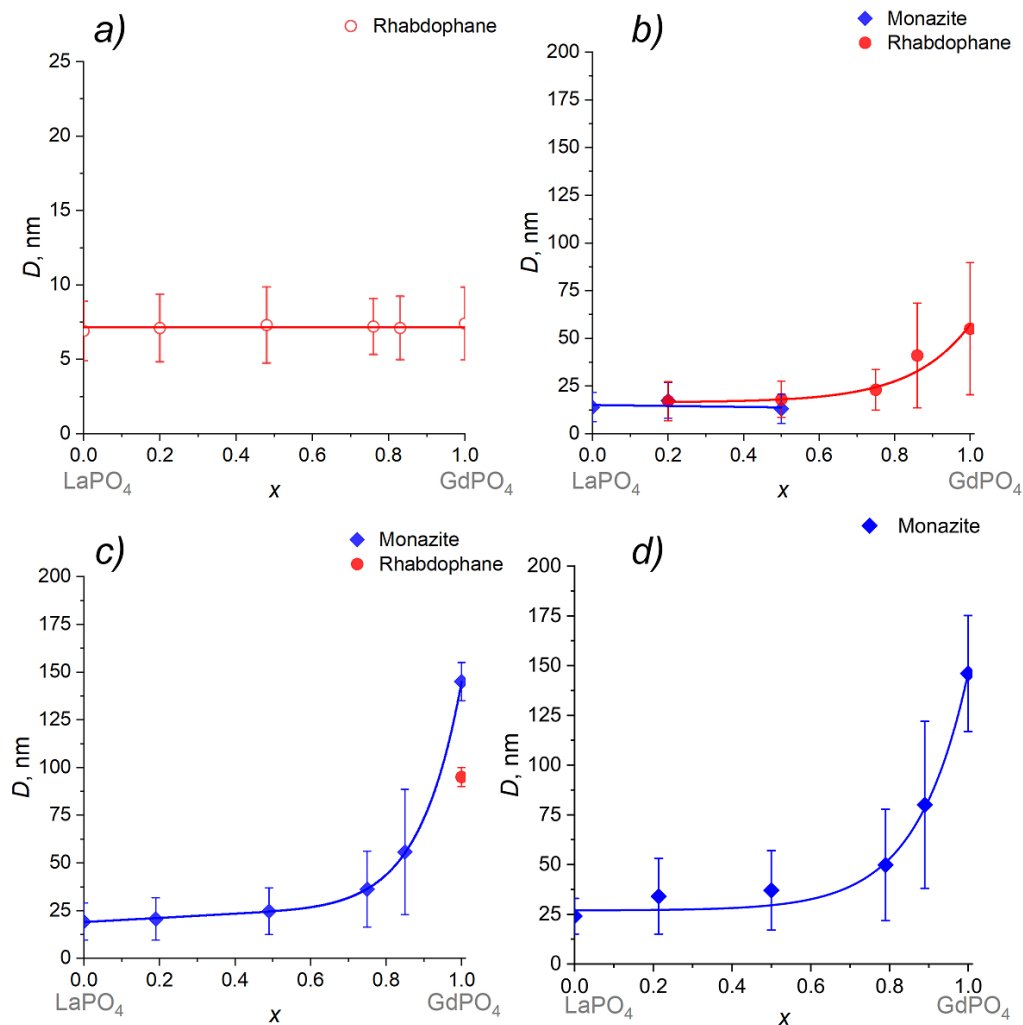
FIG. 4. Dependences of the weighted average crystallite sizes on the composition of the system for phases with rhabdophane-like and monazite-like structures in the $La_{1-x}Gd_xPO_4 \cdot (nH_2O)$ system: *a*) precipitation, *b*) hydrothermal treatment for 2 hours, *c*) hydrothermal treatment for 3 days, *d*) hydrothermal treatment for 5 days

groups: those obtained by precipitation without heat treatment [27, 43, 53, 63, 64] and those obtained using hydrothermal methods [42, 43, 65, 66]. The mass loss for the $La_{1-x}Gd_xPO_4 \cdot nH_2O$ x=0.00–1.00 samples is approximately 10%. The temperature at which the first stage of mass loss begins is close to 125 °C for all samples, and the number of water molecules leaving the channels of the structure at this stage varies from 0.16 to 0.29, depending on the composition of the compound. It is worth noting that accurately determining the temperature at which the first stage begins is challenging due to the superposition of endothermic effects in the range from 25 °C to ~200 °C.

The second step of mass loss is the most clearly distinguished for all samples, which is also evident in the samples obtained under hydrothermal conditions [40, 42, 43, 65]. The temperature at the onset of the second step shows a linear dependence on the composition of the compound, increasing from approximately 160 °C for sample x=1.00 to approximately 200 °C for sample x=0.00 (Fig. 7b). During the second step, approximately n=0.47 molecule of water leaves channels of the structure. Moreover, analysis of data [42] obtained for individual REE orthophosphates with the rhabdophane structure demonstrates a close match between the value of n≈0.47 molecule H_2O at the second step of mass loss and the literature data.

The third stage of mass loss in all compounds corresponds to an exothermic effect on the DTA curve. It appears that, during this step, in addition to the removal of water from the rhabdophane-like structure, the decomposition of impurity compounds (for example, hydroxides) and the crystallization of the X-ray amorphous phase occur. The temperature at the onset of the third step of mass loss is related to the second step and follows a linear dependence, exhibiting lower values when $LaPO_4$ is replaced with $GdPO_4$. Based on these data, it was determined that the water content in the rhabdophane-like structure for samples obtained by precipitation depends on the composition of the compounds and decreases with a reduction in the ionic radius of the REE. The TG curves show a distinguishable third step [27, 43, 51, 63, 64], associated with the removal of water from the rhabdophane-like structure, in contrast to the samples obtained through
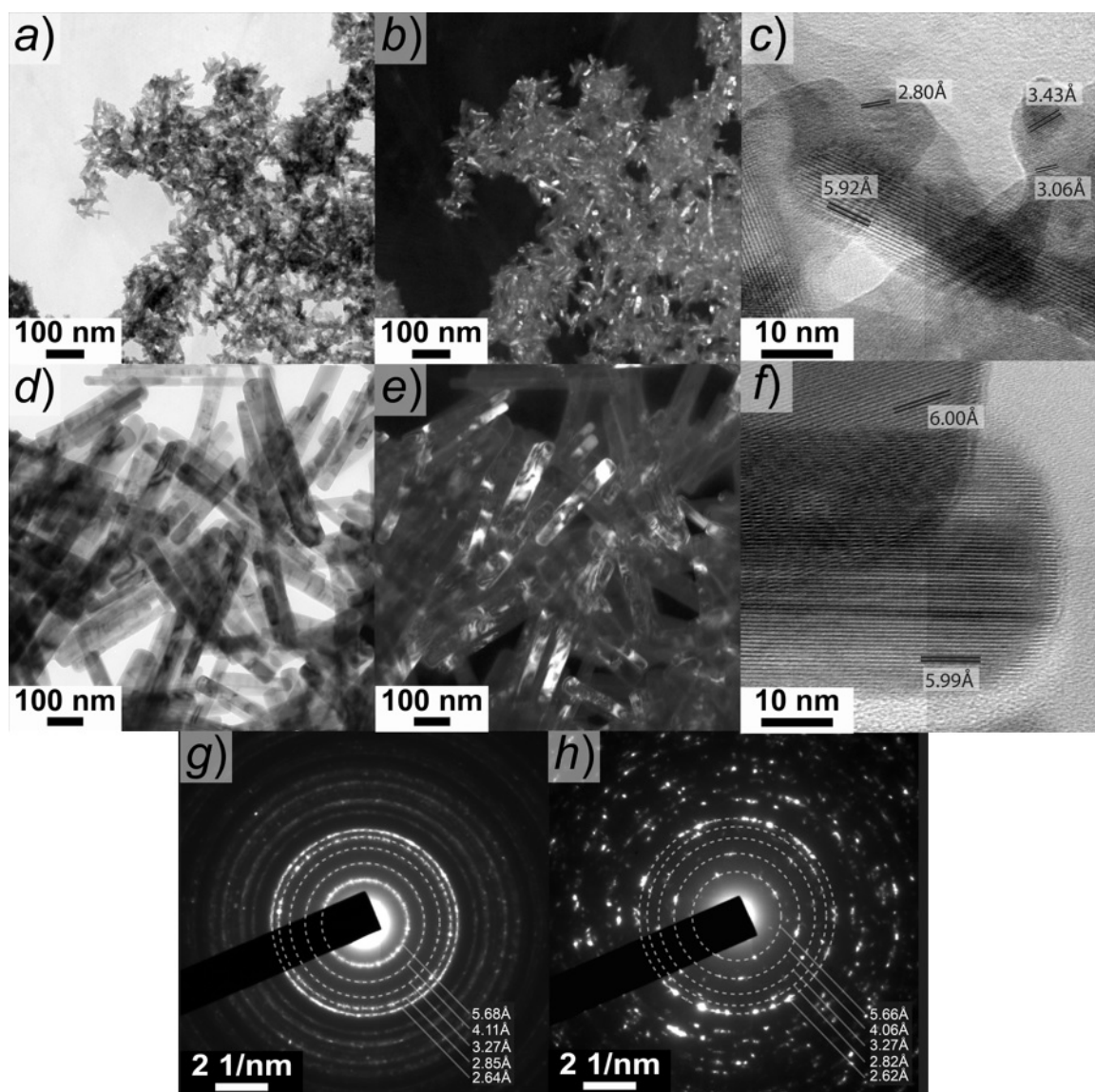
FIG. 5. Bright-field, dark-field, and high-resolution TEM images of the x=1.00 samples are presented as follows: (a–c) samples obtained by the precipitation, (d–f) samples obtained under hydrothermal conditions for 2 hours, (g) electron diffraction of the x=1.00 sample obtained by the precipitation, and (h) electron diffraction of the x=1.00 sample obtained under hydrothermal conditions for 2 hours

hydrothermal treatment. The onset temperature of the exothermic effect, occurring at $T \geq 600$ °C, is connected to the transition of the rhabdophane-like phase to the monazite-like phase. As lanthanum phosphate is substituted by gadolinium phosphate in the solid solution series $La_{1-x}Gd_xPO_4 \cdot nH_2O$, the onset transformation temperature increases from 601 °C to 733 °C, indicating that the thermal stability of $GdPO_4 \cdot nH_2O$ with the rhabdophane-like structure is greater than that of $LaPO_4 \cdot nH_2O$. A similar dependence of the transformation temperature on ionic radius in the rhabdophane-like structure is noted in references [42, 43].

The results of the TG study of samples x=0.00 and x=1.00, which were calcined at 300–400 °C for 5 minutes, in both dynamic and quasi-isothermal modes, are shown in Fig. 6a,b. Three steps of mass loss are evident on the TG curves obtained under dynamic heating conditions. At the first stage, $n \approx 0.20$ water molecules per formula unit are lost for both samples; at the second stage, $n \approx 0.30$ water molecules are lost. These values are slightly lower than those for the samples without heat treatment (Table S2), which is likely due to the absence of impurity compounds in the heat-treated samples. The third step of mass loss in samples x=0.00 and x=1.00 differs slightly. In this regard, the boundary between the second and third steps for sample x=1.00 (Fig. 8b) is more distinctly defined than for sample x=0.00 (Fig. 8a). The number of water molecules released from the rhabdophane-like structure during the heating process in the third stage varies between the two compounds: n=0.35 for lanthanum orthophosphate (Fig. 8a) and n=0.21 for gadolinium orthophosphate (Fig. 8b). The total amount of water in the rhabdophane structure is n=0.88 for $LaPO_4 \cdot nH_2O$ and n=0.72 for $GdPO_4 \cdot nH_2O$, which
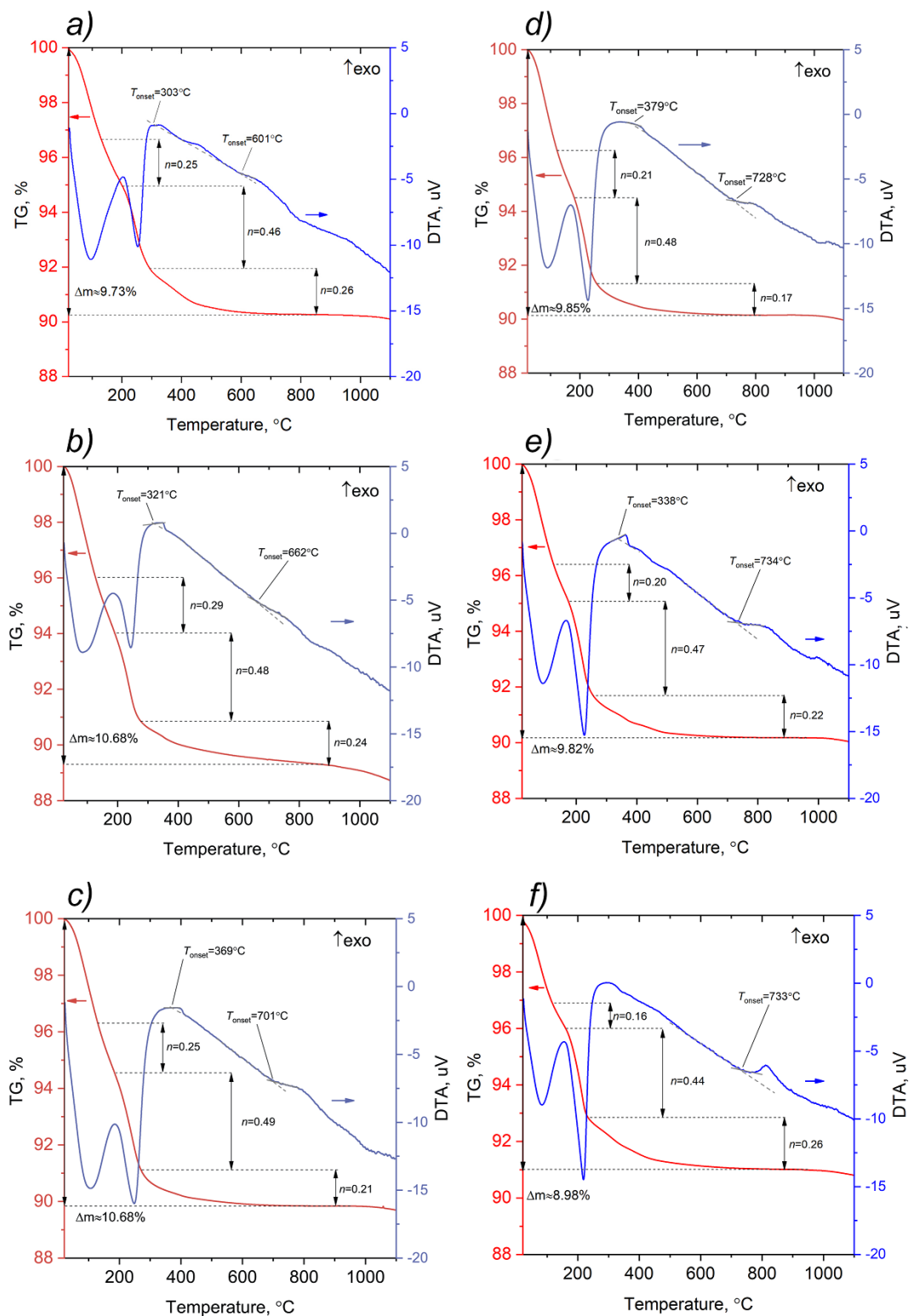
FIG. 6. DTA/TG study of samples in the $La_{1-x}Gd_xPO_4 \cdot nH_2O$ system with the rhabdophane-like structure, obtained by the precipitation method: $a)x$=0.00, $b)x$=0.20, $c)x$=0.48, $d)x$=0.76, $e)x$=0.83, $f)x$=1.00
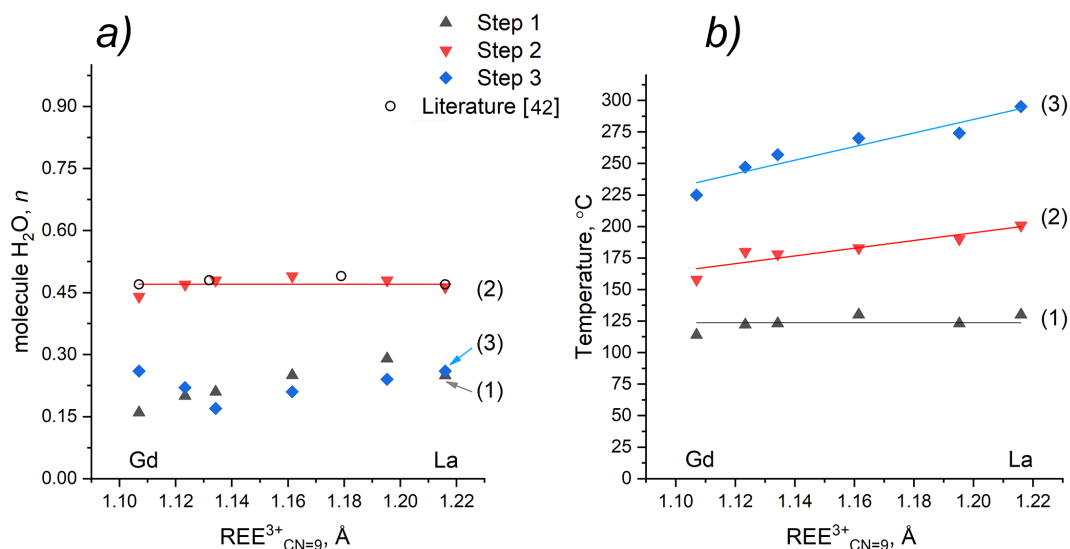
FIG. 7. *a*) The number of water molecules (*n*) in the rhabdophane structure, determined from the mass loss at each step and *b*) The temperature at which each step of mass loss begins, depending on the composition

correlates with the trend presented in Table S2, a decrease in the ionic radius of the REE leads to a reduction in the amount of water in the structure for samples obtained by the precipitation method.
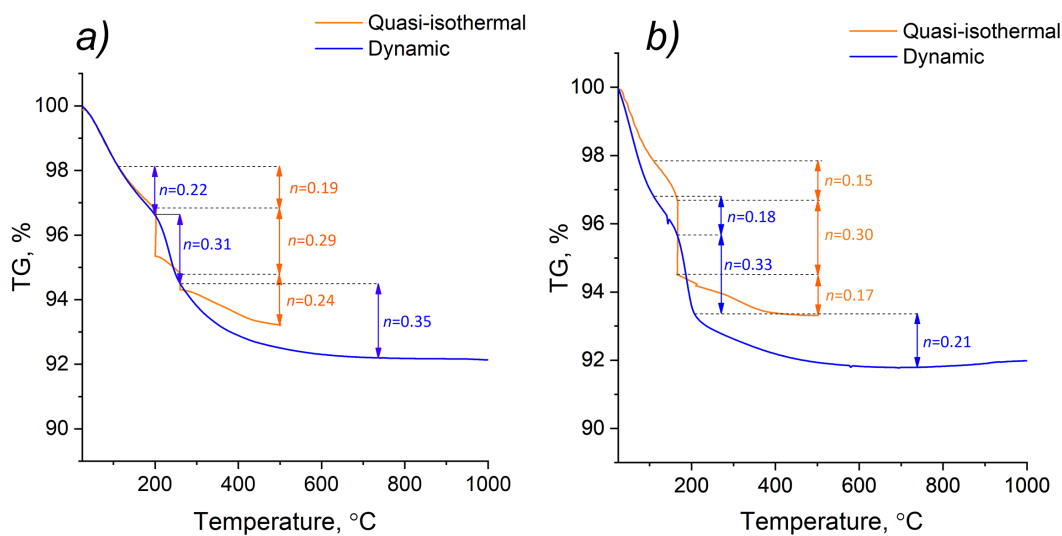

FIG. 8. DTA/TG data obtained in quasi-isothermal and dynamic modes for samples: *a*) *x*=0.00, *b*) *x*=1.00

When studying the samples with the rhabdophane-like structure at *x*=0.00 and *x*=1.00 in quasi-isothermal mode, it was found that isothermal holding at 200 °C for the *x*=0.00 sample and at 160 °C for the *x*=1.00 sample results in a sharp mass loss. This mass loss, when recalculated for the formula unit of the compounds, is approximately 0.30 molecule of water. After this loss, the mass of the samples reaches a plateau. The obtained values are in good agreement with data from the dynamic mode. Subsequently, the samples were continuously heated to the temperature at which the third step of mass loss begins (Table S2): *T*=260 °C for the *x*=0.00 sample and *T*=210 °C for the *x*=1.00 sample. Increasing the temperature at a constant rate to these specified values results in a decrease in the mass of the samples with the structure of rhabdophane-like, while quasi-isothermal holding at the same temperatures does not affect the mass change. Further heating of the samples to 500 °C after the isothermal stage (*T*=260 °C for the *x*=0.00 sample and *T* =210 °C for the *x*=1.00) is characterized by a mass loss.

These observations indicate that the third step of mass loss is initiated by an increase in sample temperature and is associated with the characteristics of the chemical bonding of water molecules in the rhabdophane structure. The number of water molecules lost per formula unit during the third step is *n*=0.24 for the *x*=0.00 sample and *n*=0.17 for the *x*=1.00 sample. According to the quasi-isothermal TG mode, the total number of water molecules in the rhabdophane structure

for $LaPO_4 \cdot nH_2O$ and $GdPO_4 \cdot nH_2O$ is $n=0.72$ and $n=0.62$, respectively. These values are lower than those determined in the dynamic heating mode, likely due to incomplete removal of water from the rhabdophane structure, as the water removal process can extend up to 600–650 °C.

Based on the data obtained from DTA/TG and TEM, it can be inferred that the samples with the rhabdophane-like structure synthesized by precipitation may contain a different number of water molecules compared to those synthesized under hydrothermal conditions. This inference is supported by the distinct shapes of the TG curves for the samples before and after hydrothermal treatment. For the samples obtained through precipitation, at least three stages of mass loss were identified, which are associated with the removal of water molecules from the channels of structure. In contrast, compounds with the rhabdophane structure that were synthesized under hydrothermal conditions primarily exhibit two stages of mass loss. The first of these stages corresponds to the loss of adsorbed water on the surface of nanoparticles. As mentioned earlier, the samples with the rhabdophane-like structure, $LaPO_4 \cdot nH_2O$ and $GdPO_4 \cdot nH_2O$, obtained via the precipitation method can contain at least 0.62 water molecules per formula unit (excluding the adsorbed water), whereas the hydrothermally synthesized samples contain approximately 0.48–0.50 water molecules (also excluding surface-bound water). Additionally, TEM studies reveal slight differences in interplanar distances for $GdPO_4 \cdot nH_2O$ samples obtained by the precipitation method compared to those subjected to hydrothermal treatment. This difference may be related to structural rearrangements caused by the varying amounts of water incorporated within the structure.

4. Conclusion

It is demonstrated that a continuous series of $La_{1-x}Gd_xPO_4 \cdot nH_2O$ ($0.00 \leq x \leq 1.00$) solid solutions with a rhabdophane-like structure and crystallite sizes ranging from 4 to 7 nm can be synthesized by precipitation in the $LaPO_4$–$GdPO_4$–H_2O system. According to TEM data, the average thickness of nanoparticles with the rhabdophane structure for the sample with $x=1.00$ correlates well with the weighted average crystallite sizes obtained both before and after hydrothermal treatment, indicating that these particles exhibit a single-crystal structure.

After hydrothermal treatment at 230 °C for 2 hours, phases containing both monazite-like and rhabdophane-like structures are formed within the system. In the two-phase region of phase coexistence ($0.20 \leq x \leq 0.75$), the weighted average values of the crystallite sizes and the chemical compositions of both phases are found to be consistent. It is noteworthy that the structural transformation occurs more slowly for compounds with a higher $GdPO_4$ content. The transformation from the rhabdophane phase to the monazite phase in the $LaPO_4$–$GdPO_4$–H_2O system occurs under hydrothermal conditions at 230 °C over a period of 5 days of isothermal holding. DTA/TG indicates that the samples obtained through the precipitation method contain approximately 1.5% of an X-ray amorphous phase along with impurity compounds.

Furthermore, it is shown that the onset temperature for the structural transformation from rhabdophane to monazite, as well as the onset temperature for each stage of mass loss (dehydration of the rhabdophane structure), and the number of water molecules in the rhabdophane-like structure, are dependent on the chemical composition of the compound. Notably, the thermal stability of $GdPO_4 \cdot nH_2O$ with the rhabdophane structure is higher than that of $LaPO_4 \cdot nH_2O$ ($\sim$733 °C versus $\sim$601 °C). However, the onset temperature for the dehydration of $GdPO_4 \cdot nH_2O$ at the second stage of mass loss is lower than that of $LaPO_4 \cdot nH_2O$ ($\sim$160 °C versus $\sim$200 °C), and the number of water molecules per formula unit is greater in $LaPO_4 \cdot nH_2O$ ($n=0.72$) than in $GdPO_4 \cdot nH_2O$ ($n=0.62$).

References

[1] Feng R., Qi Y., Liu S., Cui L., Dai Q., Bai C. Production of renewable 1,3-pentadiene over $LaPO_4$ via dehydration of 2,3-pentanediol derived from 2,3-pentanedione. *Applied Catalysis A: General*, 2022, **633**, P. 118514.

[2] Lohmann R., Cousins I.T., DeWitt J.C., Glüge J., Goldenman G., Herzke D., Lindstrom A.B., Miller M.F., Ng C.A., Patton S., Scheringer M., Trier X., Wang Z. Are Fluoropolymers Really of Low Concern for Human and Environmental Health and Separate from Other PFAS? *Environmental Science & Technology*, 2020, **54**(20), P. 12820–12828.

[3] Zhang Y.F., Dai B., Zhao D., Zhang D.H., Xu M.X., He X.H., Chen C. Promotion Effect of $PrPO_4$ for Hydrogenation Transformation of Biomass-derived Compounds over Pr-Ni-P Composites. *Materials Advances*, 2021, **2**(12), P. 3927–3939.

[4] Majhi K.C., Yadav M. Facile hydrothermal synthesis of rare earth phosphate for boosting hydrogen evolution reaction. *International Journal of Hydrogen Energy*, 2022, **47**(30), P. 14092–14103.

[5] Liu D., Wang J., Wang J., Liu K., Wen J., Xu J., Jiang P. Temperature dependences of phase composition, densification, and thermal/chemical stability of $Sr_{0.5}Zr_2(PO_4)_3$-$Nd_{0.5}Sm_{0.5}PO_4$ composite ceramics for nuclear waste form. *Journal of the European Ceramic Society*, 2024, **44**(16), P. 116806.

[6] Vance E.R., Zhang Y., McLeod T., Davis J. Actinide valences in xenotime and monazite. *Journal of Nuclear Materials*, 2011, **409**(3), P. 221–224.

[7] Thust A., Hirsch A., Haussühl E., Schrodt N., Loison L., Schott P., Peters L., Roth G., Winkler B. Physical properties and microstructures of $La_{1-x}Pr_xPO_4$ monazite-ceramics. *Physics and Chemistry of Minerals*, 2018, **45**, P. 323–332.

[8] Burakov B.E., Yagovkina M.A., Zamoryanskaya M.V., Petrova M.A., Domracheva Y.V., Kolesnikova E.V., Nikolaeva L.D., Garbuzov V.M., Kitsay A.A., Zirlin V.A. *Behavior of Actinide Host-Phases Under Self-irradiation: Zircon, Pyrochlore, Monazite, and Cubic Zirconia Doped with Pu-238*. In: Krivovichev, S.V. (eds) Minerals as Advanced Materials I. Springer, Berlin, Heidelberg, 2008.

[9] Bermudez S., Rojas J.V. Tunable X-ray-induced luminescence in lanthanide-doped $LaPO_4$ nanoparticles. *Ceramics International*, 2024, **50**(9) Part 1, P. 16076–16087.

[10] Wu J., Wu B., Wang Q., Liu Z., Hu Y., Feng F., Li J., Zhang X., Xie R. Tuning and high temperature fluorescence properties of $LaPO_4$:Sm^{3+} nanophosphors. *Optical Materials*, 2024, **153**, P. 115556.

[11] Ouertani G., Maciejewska K., Piotrowski W., Horchani-Naifer K., Marciniak L., Ferhi M. High thermal stability of warm white emitting single phase $GdPO_4$: Dy^{3+}/Sm^{3+} phosphor for UV excited wLEDs. *Journal of Luminescence*, 2024, **265**, P. 120228.

[12] Orekhova K., Burakov B., Silantieva E., Kitsay A., Popova T., Yagovkina M., Zamoryanskaya M. Synthesis and cathodoluminescence of YPO$_4$ and LuPO$_4$ single crystals activated with Er^{3+}. *Journal of Alloys and Compounds*, 2023, **968**, P. 171961.

[13] Correcher V., Boronat C., Garcia-Guinea J., Benavente J.F., Rivera-Montalvo T. Thermoluminescence characterization of natural and synthetic irradiated Ce-monazites. *Journal of Rare Earths*, 2024, **42**(4), P. 643–650.

[14] Hikichi Y., Ota T., Hattori T. Thermal, mechanical and chemical properties of sintered monazite-(La, Ce, Nd or Sm). *Mineralogical Journal*, 1997, **19**(3), P. 123–130.

[15] Zhao Z., Chen H., Xiang H., Dai F.-Z., Wang X., Peng Z., Zhou Y. (La$_{0.2}$Ce$_{0.2}$Nd$_{0.2}$Sm$_{0.2}$Eu$_{0.2}$)PO$_4$: A high-entropy rare-earth phosphate monazite ceramic with low thermal conductivity and good compatibility with Al$_2$O$_3$. *Journal of Materials Science & Technology*, 2019, **35**(12), P. 2892–2896.

[16] Du A., Wan C., Qu Z., Wu R., Pan W. Effects of Texture on the Thermal Conductivity of the LaPO$_4$ Monazite. *Journal of the American Ceramic Society*, 2010, **93**(9), P. 2822–2827.

[17] Enikeeva M.O., Proskurina O.V., Motaylo E.S., Gusarov V.V. The influence of condition of the monazite structured La$_{0.9}$Y$_{0.1}$PO$_4$ nanocrystals sintering on thermal and mechanical properties of the material. *Nanosystems: physics, chemistry, mathematics*, 2021, **12**(6), P. 799–807.

[18] Dacheux N., Clavier N., Podor R. Versatile Monazite: Resolving geological records and solving challenges in materials science. Monazite as a promising long-term radioactive waste matrix: Benefits of high-structural flexibility and chemical durability. *American Mineralogist*, 2013, **98**(5-6), P. 833–847.

[19] Van Hoozen C.J., Gysi A.P., Harlov D.E. The solubility of monazite (LaPO$_4$, PrPO$_4$, NdPO$_4$, and EuPO$_4$) endmembers in aqueous solutions from 100 to 250? ° C. *Geochimica et Cosmochimica Acta*, 2020, **280**, P. 302–316.

[20] Mikhailov D.A., Potanina E.A., Orlova A.I., Nokhrin A.V., Boldin M.S., Belkin O.A., Sakharov N.V., Skuratov V.A., Kirilkin N.S., Chuvil'deev V.N. Radiation Resistance and Hydrolytic Stability of Y$_{0.95}$Gd$_{0.05}$PO$_4$-Based Ceramics with the Xenotime Structure. *Inorganic Materials*, 2021, **57**, P. 760–765.

[21] Gysi A.P., Harlov D. Hydrothermal solubility of TbPO$_4$, HoPO$_4$, TmPO$_4$, and LuPO$_4$ xenotime endmembers at pH of 2 and temperatures between 100 and 250 °C. *Chemical Geology*, 2021, **567**, P. 120072.

[22] Lender T., Murphy G., Bazarkina E., Bukaemskiy A., Gilson S., Henkes M., Hennig C., Kaspor A., Marquardt J., Nießen J., Peters L., Poonoosamy J., Rossberg A., Svitlyk V., Kvashnina K.O., Huittinen N. Investigation of Radiation Damage in the Monazite-Type Solid Solution La$_{1-x}$Ce$_x$PO$_4$. *Inorganic Chemistry*, 2024, **63**(38), P. 17525–17535.

[23] Nasdala L., Akhmadaliev S., Burakov B.E., Chanmuang N C., Škoda R. The absence of metamictisation in natural monazite. *Scientific Reports*, 2020, **10**, P. 14676.

[24] Hikichi Y., Nomura T. Melting Temperatures of Monazite and Xenotime. *Journal of the American Ceramic Society*, 1987, **70**(10), P. 252–253.

[25] Bondar I.A., Mezentseva L.P. Single crystals of rare-earth oxides: Constitution and properties. *Progress in Crystal Growth and Characterization*, 1988, **16**, P. 81–141.

[26] Enikeeva M.O., Proskurina O.V., Gusarov V.V. Phase Diagram and Metastable Phases in the LaPO$_4$–YPO$_4$–(H$_2$O) System. *Russian Journal of Inorganic Chemistry*, 2024.

[27] Gysi A.P., Hurtig N.C., Juan Han H., Kindall E.C., Guo X., Kulik D.A., Dan Miron G. Reaction calorimetry and structural crystal properties of non-ideal binary rhabdophane solid solutions (Ce$_{1-x}$REE$_x$PO$_4 \cdot n$H$_2$O). *Geochimica et Cosmochimica Acta*, 2024.

[28] Qin D., Mesbah A., Gausse C., Szenknect S., Dacheux N., Clavier N. Incorporation of thorium in the rhabdophane structure: Synthesis and characterization of Pr$_{1-2x}$Ca$_x$Th$_x$PO$_4 \cdot n$H$_2$O solid solutions. *Journal of Nuclear Materials*, 2017, **492**, P. 88–96.

[29] Monjid A.El., Szenknect S., Mesbah A., Hunault M.O.J.Y., Menut D., Clavier N., Dacheux N. Incorporation of U(iv) in monazite–cheralite ceramics under oxidizing and inert atmospheres. *Dalton Transactions*, 2024, **53**, P. 2252–2264.

[30] Zhao X., Wang W., Teng Y., Li Y., Ma X., Liu Y., Ahuja R., Luo W., Zhang Z. Incorporation of Th^{4+} and Sr^{2+} into Rhabdophane/Monazite by Wet Chemistry: Structure and Phase Stability. *Inorganic Chemistry*, 2023, **62**(38), P. 15605–15615.

[31] Chong S., J. Riley B., Lu X., Du J., Mahadevan T., Hegdec V. Synthesis and properties of anhydrous rare-earth phosphates, monazite and xenotime: a review. *RSC Advances*, 2024, **14**, P. 18978–19000.

[32] Rafiuddin M.R., Guo S., Donato G., Grosvenor A.P., Dacheux N., Cava R.J., Mesbah A. Structural and magnetic properties of churchite-type REPO$_4 \cdot 2$H$_2$O materials. *Journal of Solid State Chemistry*, 2022, **312**, P. 123261.

[33] Rafiuddin M.R., Tyagi C., Haq M.A. Synthesis and structural investigation of churchite-type REPO$_4 \cdot 2$H$_2$O (RE = Y, Gd, Dy) nanocrystals. *Journal of Solid State Chemistry*, 2022, **311**, P. 123150.

[34] Enikeeva M.O., Proskurina O.V., Gerasimov E.Yu., Nevedomskiy V.N., Gusarov V.V. Synthesis under hydrothermal conditions and structural transformations of nanocrystals in the LaPO$_4$-YPO$_4$-(H$_2$O) system. *Nanosystems: physics, chemistry, mathematics*, 2023, **14**(6), P. 660–671.

[35] Bamforth T.G., Xia F., Putnis A., Brugger J., Hu S.-Y., Roberts M.P., Suvorova A., Pring A. Hydrothermal mineral replacement in the apatite-rhabdophane-monazite system: Experiments, reaction mechanisms and geological implications. *Chemical Geology*, 2024, **666**, P. 122307.

[36] Subramani T., Rafiuddin M.R., Shelyug A., Ushakov S., Mesbah A., Clavier N., Qin D., Szenknect S., Elkaim E., Dacheux N., Navrotsky A. Synthesis, Crystal Structure, and Enthalpies of Formation of Churchite-type REPO$_4 \cdot 2$H$_2$O (RE = Gd to Lu) Materials. *Crystal Growth & Design*, 2019, **19**(8), P. 4641–4649.

[37] Kohlmann M., Sowa H., Reithmayer K., Schulz H., Krüger R.-R., Abriel W. Structure of a Y$_{1-x}$(Gd,Dy,Er)$_x$PO$_4 \cdot 2$H$_2$O microcrystal using synchrotron radiation. *Acta Crystallographica section C*, 1994, C**50**, P. 1651–1652.

[38] Ivashkevich L.S., Lyakhov A.S., Selevich A.F. Preparation and structure of the yttrium phosphate dihydrate YPO$_4 \cdot 2$H$_2$O. *Phosphorus Research Bulletin*, 2013, **28**, P. 45–50.

[39] Roncal-Herrero T., Rodríguez-Blanco J.D., Oelkers E.H., Benning L.G. The direct precipitation of rhabdophane (REEPO$_4 \cdot n$H$_2$O) nano-rods from acidic aqueous solutions at 5–100 °C. *Journal of Nanoparticle Research*, 2011, **13**, P. 4049–4062.

[40] Khalili R., Larsson A.-C., Telkki V.-V., Lantto P., Kantola A.M. Local structures of rare earth phosphate minerals by NMR. *Journal of Solid State Chemistry*, 2022, **311**, P. 123097.

[41] Mesbah A., Clavier N., Elkaim E., Gausse C., Ben Kacem I., Szenknect S., Dacheux N. Monoclinic Form of the Rhabdophane Compounds: REEPO4·0.667H$_2$O. *Crystal Growth & Design*, 2014, **14**(10), P. 5090–5098.

[42] Shelyug A., Mesbah A., Szenknect S., Clavier N., Dacheux N., Navrotsky A. Thermodynamics and Stability of Rhabdophanes, Hydrated Rare Earth Phosphates REPO$_4 \cdot n$H$_2$O. *Frontiers in Chemistry*, 2018, **6**(604), P. 1–25.

[43] Enikeeva M.O., Yakovleva A.A., Proskurina O.V., Nevedomskiy V.N., Gusarov V.V. Phase formation under hydrothermal conditions and thermal transformations in the GdPO$_4$-YPO$_4$-H$_2$O system. *Inorganic Chemistry Communications*, 2024, **159**, P. 111777.

[44] Mooney R.C.L. Crystal Structures of a Series of Rare Earth Phosphates. *Journal of Chemical Physics*, 1948, **16**, P. 1003.

[45] Mooney R.C.L. X-ray diffraction study of cerous phosphate and related crystals. I. Hexagonal modification. *Acta Crystallographica*, 1950, **3**, P. 337–340.

[46] Enikeeva M.O., Proskurina O.V., Levin A.A., Smirnov A.V., Nevedomskiy V.N., Gusarov V.V. Structure of $Y_{0.75}La_{0.25}PO_4 \cdot 0.67H_2O$ rhabdophane nanoparticles synthesized by the hydrothermal microwave method. *Journal of Solid State Chemistry*, 2023, **319**, P. 123829.

[47] Weiss H., Bräu M. F. How Much Water Does Calcined Gypsum Contain? *Angewandte Chemie International Edition*, 2009, **48**(19), P. 3520–3524.

[48] Duran E.C., Rafiuddin M.R., Shen Y., Hunt S.A., Haq Mirc A., Eggemana A.S. 3D electron diffraction studies of synthetic rhabdophane (DyPO$_4$ · nH$_2$O). *Acta Crystallographica section C*, 2024, **81**, Part 10, P. 612–619.

[49] Hikichi Y., Murayama K., Ohsato H., Nomura T. Thermal Changes of Rare Earth Phosphate Minerals. *Journal of the Mineralogical Society of Japan*, 1990, **19**(3), P. 117–126.

[50] Hikichi Y., Ota T., Hattori T., Imaeda T. Synthesis and thermal reactions of rhabdophane-(Y). *Mineralogical Journal*, 1996, **18**(3), P. 87–96.

[51] Boakye E.E., Mogilevsky P., Hay R.S. Synthesis of Nanosized Spherical Rhabdophane Particles. *Journal of the American Ceramic Society*, 2005, **88**(10), P. 2740–2746.

[52] Vanetsev A.S., Samsonova E.V., Gaitko O.M., Keevend K., Popov A.V., Mäeorg U., Mändar H., Sildos I., Orlovskii Yu.V. Phase composition and morphology of nanoparticles of yttrium orthophosphates synthesized by microwave-hydrothermal treatment: The influence of synthetic conditions. *Journal of Alloys and Compounds*, 2015, **639**, P. 415–421.

[53] Kijkowska R. Thermal decomposition of lanthanide orthophosphates synthesized through crystallisation from phosphoric acid solution. *Thermochimica Acta*, 2003, **404**(1-2), P. 81–88.

[54] Lucas S., Champion E., Bernache-Assollant D., Leroy G. Rare earth phosphate powders RePO$_4$ · nH$_2$O (Re=La, Ce or Y) II. Thermal behavior. *Journal of Solid State Chemistry*, 2004, **177**(4-5), P. 1312–1320.

[55] Jonasson R.G., Vance E.R. DTA study of the rhabdophane to monazite transformation in rare earth (La-Dy) phosphates. *Thermochimica Acta*, 1986, **108**, P. 65–72.

[56] Ochiai A., Utsunomiya S. Crystal Chemistry and Stability of Hydrated Rare-Earth Phosphates Formed at Room Temperature. *Minerals*, 2017, **7**(5), P. 84.

[57] Mesbah A., Clavier N., Elkaim E., Szenknect S., Dacheux N. In pursuit of the rhabdophane crystal structure: from the hydrated monoclinic LnPO$_4$0.667H$_2$O to the hexagonal LnPO$_4$ (Ln = Nd, Sm, Gd, Eu and Dy). *Journal of Solid State Chemistry*, 2017, **249**, P. 221–227.

[58] J. Livage, "Vers une chimie écologique. Quand l'air et l'eau remplacent le pétrole", Le Monde, 1977.

[59] Skogareva L.S., Kottsov S.Yu., Shekunova T.O., Baranchikov A.E., Ivanova O.S., Yapryntsev A.D., Ivanov V.K. Selective precipitation of rare earth orthophosphates with hydrogen peroxide from phosphoric acid solutions. *Russian Journal of Inorganic Chemistry*, 2017, **62**, P. 1141–1146.

[60] Elovikov D.P., Nikiforova K.O., Tomkovich M.V., Proskurina O.V., Gusarov V.V. The pH value influence on the waylandite-structured BiAl$_3$(PO$_4$)$_2$(OH)$_6$ compound formation under hydrothermal conditions. *Inorganica Chimica Acta*, 2024, **561**, P. 121856.

[61] Khrapova E.K., Ivanova A.A., Kirilenko D.A., Levin A.A., Bert N.A., Ugolkov V.L., Krasilin A.A. Phase transformations of (Co$_x$Mg$_{1-x}$)$_3$Si$_2$O$_5$(OH)$_4$ phyllosilicate nanoscrolls upon heating in Ar, O$_2$ and H$_2$ containing atmospheres. *Applied Clay Science*, 2024, **250**, P. 107282.

[62] Rietveld H.M. A profile refinement method for nuclear and magnetic structures. *Journal of Applied Crystallography*, 1969, **2**, P. 65–71.

[63] Anfimova T., Li Q., Jensen J.O., Bjerrum N.J. Thermal Stability and Proton Conductivity of Rare Earth Orthophosphate Hydrates. *International Journal of Electrochemical Science*, 2014, **9**(5), P. 2285-2300.

[64] Maslennikova T.P., Osipov A.V., Mezentseva L.P., Drozdova I.A., Kuchaeva S.K., Ugolkov V.L., Gusarov V.V. Synthesis, mutual solubility, and thermal behavior of nanocrystals in the LaPO$_4$-YPO$_4$-H$_2$O system. *Glass Physics and Chemistry*, 2010, **36**, P. 351–357.

[65] Patra C.R., Gabashvili A., Patra S., Jacob D.S., Gedanken A., Landaua A., Gofer Y. Microwave approach for the synthesis of rhabdophane-type lanthanide orthophosphate (Ln = La, Ce, Nd, Sm, Eu, Gd and Tb) nanorods under solvothermal conditions. *New Journal of Chemistry*, 2005. **29**(5), P. 733–739.

[66] Zhao X., Teng Y., Li Y., Zheng X., Zheng Q., Ma R., Liu G., Liu Y., Ahuja R., Luo W. Response of Nd^{3+} and Sm^{3+} precipitating into rhabdophane and the leaching mechanism of associated monazite ceramics. *Journal of the American Ceramic Society*, 2022, **106**(2), P. 1287–1298.

Information about the authors:

Maria O. Enikeeva – Ioffe Institute, 194021 St. Petersburg, Russia; Branch of Petersburg Nuclear Physics Institute named after B.Ṗ. Konstantinov of National Research Centre "Kurchatov Institute" – Institute of Silicate Chemistry, 199034, St. Petersburg, Russia; ORCID 0000-0002-9633-4421; i@odin2tri.ru

Kseniya A. Zhidomorova – Branch of Petersburg Nuclear Physics Institute named after B.Ṗ. Konstantinov of National Research Centre "Kurchatov Institute" – Institute of Silicate Chemistry, 199034, St. Petersburg, Russia; St. Petersburg State Institute of Technology, 190013, St. Petersburg, Russia; ORCID 0009-0007-6447-7341; zhidomorovak@gmail.com

Dmitriy P. Danilovich – St. Petersburg State Institute of Technology, 190013, St. Petersburg, Russia; ORCID 0000-0001-7110-557X; dmitrydanilovich@gmail.com

Vladimir N. Nevedomskiy – Ioffe Institute, 194021 St. Petersburg, Russia; ORCID 0000-0002-7661-9155; nevedom@mail.ioffe.ru

Olga V. Proskurina – Ioffe Institute, 194021 St. Petersburg, Russia; St. Petersburg State Institute of Technology, 190013, St. Petersburg, Russia; ORCID 0000-0002-2807-375X; proskurinaov@mail.ru

Victor V. Gusarov – Ioffe Institute, 194021 St. Petersburg, Russia; ORCID 0000-0003-4375-6388; gusarov@mail.ioffe.ru
Conflict of interest: the authors declare no conflict of interest.